

Rapid adaptive optical recovery of optimal resolution over large volumes

Kai Wang¹, Daniel E Milkie², Ankur Saxena³, Peter Engerer⁴, Thomas Misgeld^{4–6}, Marianne E Bronner³, Jeff Mumm^{7,8} & Eric Betzig¹

Using a descanned, laser-induced guide star and direct wavefront sensing, we demonstrate adaptive correction of complex optical aberrations at high numerical aperture (NA) and a 14-ms update rate. This correction permits us to compensate for the rapid spatial variation in aberration often encountered in biological specimens and to recover diffraction-limited imaging over large volumes (>240 μm per side). We applied this to image fine neuronal processes and subcellular dynamics within the zebrafish brain.

Optical imaging at diffraction-limited resolution in whole living organisms, where cell-to-cell interactions have crucial roles, is difficult owing to refractive index heterogeneities arising from different cell morphologies within tissues and subcellular domains within cells. Although adaptive optics¹ (AO) using a variety of approaches has been applied to this problem^{2,3}, AO microscopy remains challenging in many specimens owing to the modal complexity and large amplitude of the wavefront aberrations encountered, as well as how quickly these aberrations change as a function of position within the specimen⁴. Here we report an AO microscope (Supplementary Fig. 1) operating either in two-photon-excitation (TPE, Figs. 1 and 2) or in

linear-confocal (Fig. 3) fluorescence mode that provides corrective updates of complex, spatially varying aberrations fast enough to recover diffraction-limited performance at 1.1 NA over large imaging volumes without observable measurement-induced photobleaching or photodamage.

The method makes use of two previously reported innovations: direct wavefront sensing with a nonlinear guide star⁵ created by TPE and descanned signal collection and measurement⁶, used in our case to measure the aberrated wavefront averaged over a small subvolume scanned by the guide star. Nonlinearity insures that the signal comes from a compact focal volume without the need

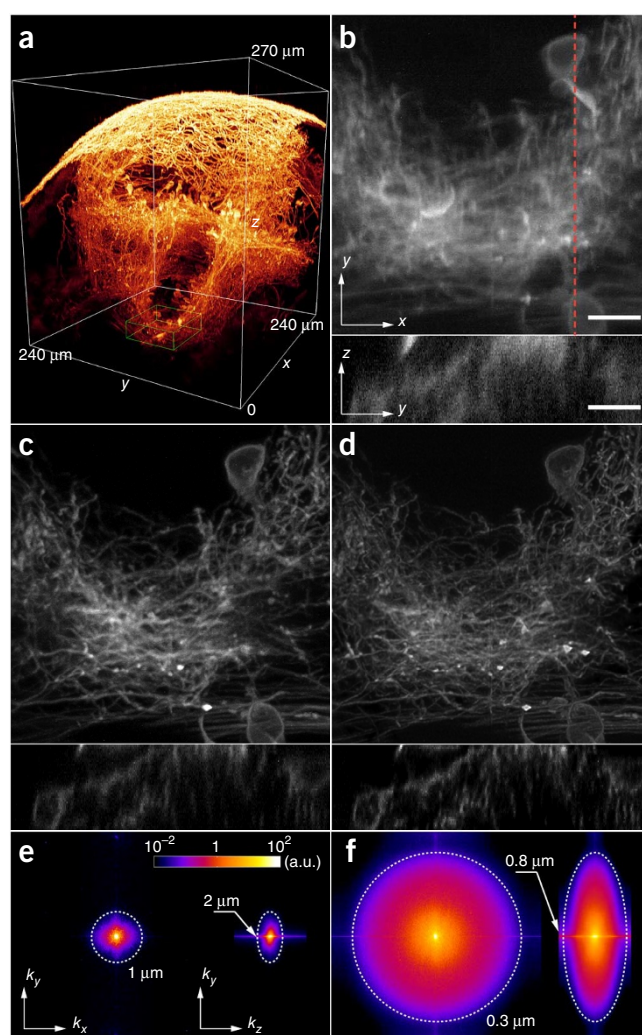
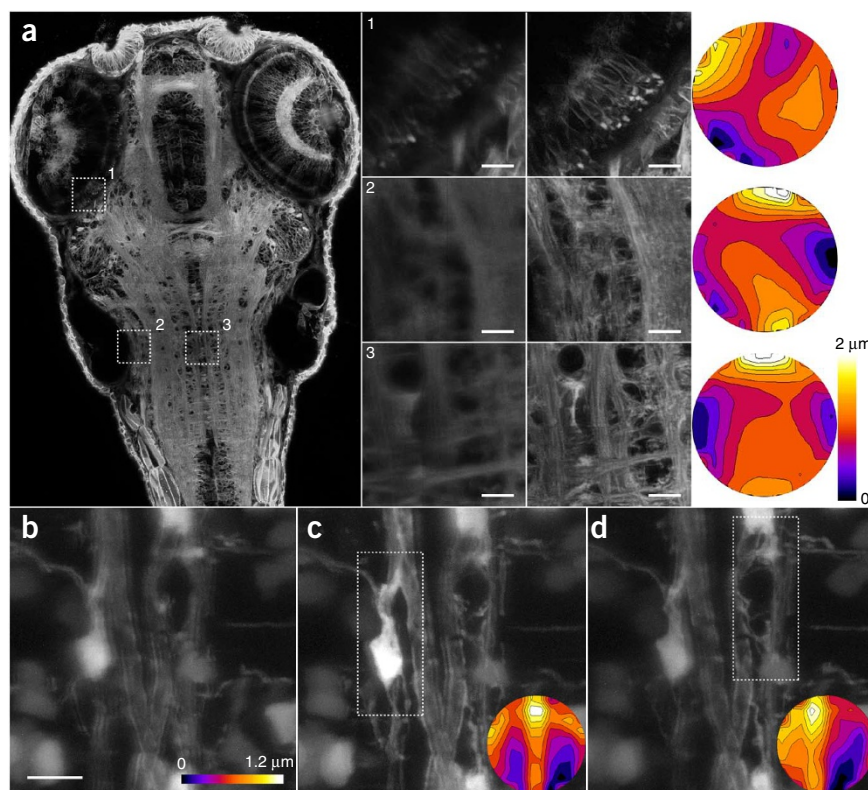


Figure 1 | AO over a large volume in the living zebrafish brain. (a) 3D rendering after AO correction of a membrane-labeled subset of neurons imaged by TPE fluorescence microscopy. (b–d) xy maximum-intensity projection (MIP, top) and an yz orthoslice (bottom), through the plane defined by the red line, of the neurons in the green box in a before AO correction (b), after AO correction (c) and after AO correction and subsequent deconvolution (d). Scale bars, 10 μm . (e, f) k_x , k_y and k_y , k_z spatial frequency representation in arbitrary units (a.u.) of the volume in b, showing substantial loss of resolution without AO (e) and the volume in d, showing recovery of spatial frequencies with AO out to the diffraction limit in all three dimensions (f).

¹Janelia Farm Research Campus, Howard Hughes Medical Institute, Ashburn, Virginia, USA. ²Coleman Technologies, Inc., Newtown Square, Pennsylvania, USA. ³Division of Biology, California Institute of Technology, Pasadena, California, USA. ⁴Institute of Neuronal Cell Biology, Technische Universität München, Munich, Germany. ⁵Munich Center for Systems Neurology, Munich, Germany. ⁶German Center for Neurodegenerative Diseases, Munich, Germany. ⁷Department of Cellular Biology and Anatomy, Georgia Regents University, Augusta, Georgia, USA. ⁸Present address: Wilmer Eye Institute, Johns Hopkins School of Medicine, Baltimore, Maryland, USA. Correspondence should be addressed to E.B. (betzige@janelia.hhmi.org).

Figure 2 | Spatial variability of aberrations across the living zebrafish brain. **(a)** xy MIP (left) after AO correction of a ubiquitously expressed cell-membrane marker as imaged by TPE fluorescence microscopy at a depth of 150 μm . Three numbered regions are shown at higher magnification before (middle left) and after (middle right) AO correction, along with the wavefront correction (right) for each. Scale bars, 10 μm . **(b)** xy MIP of oligodendrocytes close to the midline of the hindbrain in a different cell line, before AO correction. **(c,d)** Same region as in **b**, after AO correction, using the wavefront corrections (insets) measured over only the indicated subvolumes (white boxes). Scale bar, 10 μm (**b–d**).



for exogenously introduced fluorescent point sources⁷ or pinhole filtering of out-of-focus fluorescence⁸ that can also filter out much of the modal structure in the aberration. However, a fixed guide star is not by itself sufficient—many biological specimens are so heterogeneous that the wavefront can vary on a scale that is small compared to even the individual lenslets of a Shack-Hartmann (SH) sensor. This variation results in complex speckle patterns in various cells of the sensor array (Supplementary Fig. 2a), which in turn yield inaccurate measurements of the local wavefront slope and thus incomplete or incorrect AO compensation, even at the chosen corrective point (Supplementary Fig. 2d).

If, however, we scan the guide star over a small volume of similar aberration (Supplementary Fig. 2e) and *descan* the collected signal using the same pair of scanning mirrors (Supplementary Fig. 1), then a stationary wavefront is projected to the SH lenslet array wherein the finest structure specific to each excitation point is averaged out. As a result, the lenslets sample the average wavefront slope over the scan volume, and a single spot appears in each cell of the sensor (Supplementary Fig. 2b), yielding an accurate determination of the average aberration, which is usually sufficient to recover near-diffraction-limited performance over the entire scan volume. In contrast, the AO compensation for a fixed guide star, even when locally correct, often provides less-accurate correction when applied at other positions within a similar volume.

This approach is rapid, robust and minimally invasive. The entire closed-loop system of SH detection, wavefront calculation and spatial light modulator (SLM)-based correction provides new updates as fast as every 14 ms, which is essential in the scanning of large sample volumes requiring many corrective subvolumes. The method requires only a sufficient number of excitable fluorophores somewhere within each scan volume, rather than the identification of a specific fluorescent feature and subsequent targeting of the guide star. Finally, photoinduced bleaching or sample damage is mitigated because the excitation is spread over the entire scan volume rather than concentrated at a single corrective point that may in fact be the point of greatest interest.

We demonstrated the efficacy of this approach in the TPE mode by imaging a membrane-labeled subset of neurons in the brain of a living zebrafish embryo 72 h after fertilization (Fig. 1a and

Supplementary Video 1). This $240\text{ }\mu\text{m} \times 240\text{ }\mu\text{m} \times 270\text{ }\mu\text{m}$ imaging volume consists of 19,584 corrective subvolumes of $30\text{ }\mu\text{m} \times 30\text{ }\mu\text{m} \times 1.05\text{ }\mu\text{m}$ each. Deep in the midbrain (Fig. 1a) the individual neuronal processes, unresolved without AO (Fig. 1b), become distinct after correction (Fig. 1c). Indeed, whereas the optical-transfer function (OTF) before correction contains measurable spatial frequencies out to only a small fraction of the Abbe limit (Fig. 1e), the post-correction OTF is sufficiently close to the diffraction-limited one measured from fluorescent beads that deconvolution yields an accurate three-dimensional (3D) representation of the sample (Fig. 1d) at all spatial frequencies out to this limit (Fig. 1f), throughout the imaging volume.

We recovered diffraction-limited performance even though we applied an SH wavefront measurement based on the $\sim 550\text{-nm}$ emission wavelength (λ) of YFP to the SLM to correct the focus of the 960-nm excitation. The wavefront measurement occurs simultaneously with TPE imaging, so there is no need to pause for correction. Finally, the method is both fast and noninvasive enough to study subcellular dynamics with 4-min temporal resolution for extended periods in the developing embryo, as well as the neurite-guided motility of oligodendrocytes deep in the zebrafish hindbrain (Supplementary Fig. 3 and Supplementary Video 2).

The results from imaging ubiquitously labeled cell membranes in a $6\text{-}\mu\text{m}$ -thick slab at a depth of $150\text{ }\mu\text{m}$ across an entire zebrafish brain (Fig. 2 and Supplementary Video 3) underscore the spatial variability and complexity of the aberration even in this nominally transparent, optically benign model organism. For example, three widely separated regions covering (i) photoreceptors of the retina, (ii) neuropil close to the ear and (iii) neuropil in the reticular formation of the hindbrain require three very different corrective patterns, each of $\sim 3\lambda$

Figure 3 | Two-color confocal imaging with AO provided by a descanned two-photon guide star deep in the living zebrafish brain. 3D volume rendering (left) of oligodendrocytes (magenta) and neuronal nuclei (green) from the optic tectum through the midbrain. MIPs before (center) and after (right) AO correction across four subvolumes spanning depths indicated by yellow boxes (left) demonstrate the recovery of diffraction-limited resolution throughout the 200- μm -deep imaging volume.

peak-to-peak amplitude (Fig. 2a). Indeed, near the spinal cord midline, aberrations can be very complex (for example, 45 Zernike modes of amplitudes $>\lambda/10$, Supplementary Fig. 4) and change very rapidly: wavefront corrections for each of two subvolumes separated by only $\sim 15\ \mu\text{m}$ (Fig. 2c,d) are dramatically different, and each provides poor compensation of aberration when applied to the other.

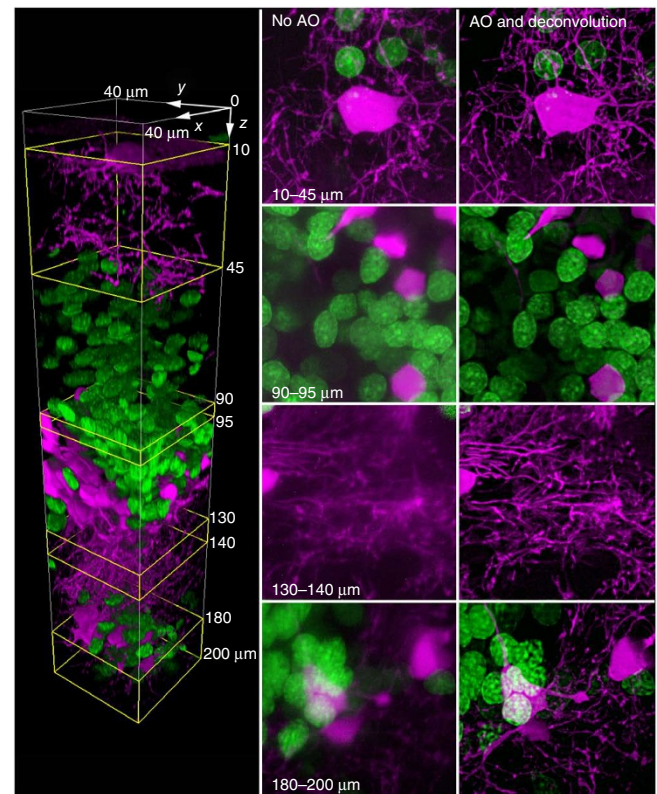
In general, it is difficult to know a priori for different organisms and different regions within an organism how to choose the dimensions of the largest possible corrective subvolume that still yields diffraction-limited performance. Fortunately, for structurally and developmentally stereotypical organisms such as zebrafish, a library of subvolume sizes obtained empirically from one sample can be validly applied to subsequent ones.

For multicolor imaging, our microscope includes a confocal mode, wherein we reflect both the scanned linear excitation and the descanned fluorescence signal off a visible-optimized SLM (Supplementary Fig. 1) to provide the necessary adaptive optical correction for each. For each subvolume, we first determine the correction itself by the descanned TPE guide star approach above, applied to a single plane at the center of the subvolume.

This confocal mode can provide multicolor near-diffraction-limited resolution over large regions of the zebrafish brain, such as oligodendrocytes and neuronal nuclei from the top of the optic tectum to a depth of 200 μm in the midbrain (Fig. 3 and Supplementary Video 4). As a result, we can now study subcellular organelles in the optically challenging environment of a living vertebrate with the clarity normally associated with isolated cultured cells. Examples include centriole pairs of centrosomes in photoreceptors of the retina (Supplementary Fig. 5a–e), and the plasma membrane and mitochondria in a neuron $\sim 150\ \mu\text{m}$ deep in the hindbrain (Supplementary Fig. 5f–h and Supplementary Video 5). Time lapse imaging of two neurons in the hindbrain at 2-min intervals shows mitochondrial dynamics in the soma and surrounding neurites (Supplementary Fig. 6 and Supplementary Video 6).

Although the confocal mode provides better resolution than the TPE mode for depths at which the scattering of visible light is negligible (Supplementary Fig. 7), the longer scattering length of infrared light makes the TPE mode applicable at greater depths. Nevertheless, for many samples, scattering will eventually render either mode unusable, as the focus of the ballistic component of the fluorescence in each cell of the SH sensor will become dominated by the unfocused background from the scattered component. In this limit, TPE imaging coupled to AO provided by indirect wavefront sensing^{9–12} provides a possible alternative.

The serial acquisition of image data in the TPE and confocal modes, rather than the AO correction, is currently the rate-limiting step in the imaging process. However, the speed and noninvasiveness of our approach make it well suited for integration with much faster parallel acquisition technologies such as



light-sheet microscopy^{13–16}, which provides good resolution at the periphery of embryos but is compromised by aberrations affecting both the independent excitation and detection pathways such that at later stages of development, it can be difficult to retain even single-cell resolution internally, much less subcellular resolution¹⁷ or super-resolution¹⁸. Indeed, combining our AO approach with nondiffracting, ultra-thin light sheets^{17,18} may permit us to study both the structural and functional^{19,20} development of complex neural circuits spanning large regions of the zebrafish brain with synaptic resolution.

METHODS

Methods and any associated references are available in the [online version of the paper](#).

Note: Any Supplementary Information and Source Data files are available in the online version of the paper.

ACKNOWLEDGMENTS

We thank our colleagues N. Ji for many fruitful technical discussions and suggestion of the zebrafish system; P. Keller for the HRAS transgenic line; C. Yang, S. Narayan, M.B. Ahrens, M. Koyama, B. Lemon, K. McDole and P. Keller for further guidance on zebrafish biology; J. Cox, M. Rose, A. Luck and J. Barber for zebrafish maintenance and breeding; and R. Kloss, B. Biddle and B. Bowers for machining services. We are grateful to R. Köster (Technical University of Braunschweig) for providing the KalTA4 transactivator and X. Xie (Georgia Regents University) for assistance in generating corresponding transgenic Enhancer Trap lines. We also thank R. Kesh (University of Bath) for the Sox10: eGFP line and U. Strahle (Karlsruhe Institute of Technology) for the Ngn:nRFP line. J.S.M. is supported by US National Institutes of Health (NIH) grants R21 MH083614 (NIMH) and R43 HD047089 (NICHD). M.E.B. is supported by NIH grant DE16459. T.M. acknowledges the financial support of the Center for Integrated Protein Sciences (EXC114 CIPS^M) and of the Munich Cluster for Systems Neurology (EXC1010 SyNergy). P.E. was supported by DFG Research Training Group 1373. A.S. and P.E. acknowledge support from the Howard Hughes Medical Institute Janelia Farm visiting scientist program.

AUTHOR CONTRIBUTIONS

E.B. supervised the project; K.W. and E.B. conceived the idea; D.E.M., K.W. and E.B. developed the instrument control program; K.W. built the instrument and performed the experiments; A.S., P.E., T.M., M.E.B. and J.M. supplied zebrafish lines and guidance on live zebrafish imaging; K.W. and E.B. analyzed the data; E.B. wrote the paper with input from all co-authors.

COMPETING FINANCIAL INTERESTS

The authors declare no competing financial interests.

Reprints and permissions information is available online at <http://www.nature.com/reprints/index.html>.

1. Hardy, J.W. *Adaptive Optics for Astronomical Telescopes* (Oxford Univ. Press, 1998).
2. Booth, M.J. *Phil. Trans. R. Soc. A* **365**, 2829–2843 (2007).
3. Kubby, J.A. *Adaptive Optics for Biological Imaging* (CRC Press, 2013).
4. Schwertner, M., Booth, M.J. & Wilson, T. *Opt. Express* **12**, 6540–6552 (2004).
5. Aviles-Espinosa, R. *et al. Biomed. Opt. Express* **2**, 3135–3149 (2011).
6. Hofer, H., Artal, P., Singer, B., Aragón, J.L. & Williams, D.R. *J. Opt. Soc. Am. A Opt. Image Sci. Vis.* **18**, 497–506 (2001).
7. Tao, X. *et al. Opt. Lett.* **36**, 1062–1064 (2011).
8. Tao, X. *et al. Opt. Lett.* **36**, 3389–3391 (2011).
9. Débarre, D. *et al. Opt. Lett.* **34**, 2495–2497 (2009).
10. Ji, N., Milkie, D.E. & Betzig, E. *Nat. Methods* **7**, 141–147 (2010).
11. Cui, M. *Opt. Lett.* **36**, 870–872 (2011).
12. Milkie, D.E., Betzig, E. & Ji, N. *Opt. Lett.* **36**, 4206–4208 (2011).
13. Keller, P.J., Schmidt, A.D., Wittbrodt, J. & Stelzer, E.H.K. *Science* **322**, 1065–1069 (2008).
14. Kaufmann, A., Mickoleit, M., Weber, M. & Husken, J. *Development* **139**, 3242–3247 (2012).
15. Tomer, R., Khairy, K. & Keller, P.J. *Curr. Opin. Genet. Dev.* **21**, 558–565 (2011).
16. Weber, M. & Husken, J. *Curr. Opin. Genet. Dev.* **21**, 566–572 (2011).
17. Planchon, T.A. *et al. Nat. Methods* **8**, 417–423 (2011).
18. Gao, L. *et al. Cell* **151**, 1370–1385 (2012).
19. Ahrens, M.B. *et al. Nature* **485**, 471–477 (2012).
20. Ahrens, M.B. *et al. Nat. Methods* **10**, 413–420 (2013).

ONLINE METHODS

Scanning adaptive optical microscope using a descanned nonlinear guide star. The microscope (**Supplementary Fig. 1**) is comprised of subsystems for two-photon near-infrared (NIR) excitation, visible fluorescence detection and wavefront measurement and continuous wave (CW) visible excitation. In the two-photon subsystem, pulsed light from a Ti:Sapphire laser (Coherent, Chameleon Ultra II), intensity controlled by a Pockels cell (Conoptics, 350-80-LA-02), is expanded to a $1/e^2$ diameter of 8 mm before being reflecting at 8° from the normal off a NIR-responsive spatial light modulator (SLM NIR, Boulder Nonlinear Systems, HSP256-1064). The SLM is used to apply the corrective pattern needed to retain a diffraction-limited two-photon excitation (TPE) focus in the specimen. A pair of NIR achromatic relay lenses (focal lengths $f_1 = 150$ mm and $f_2 = 125$ mm) operating in a $2f_1 + 2f_2$ configuration are then used to image the SLM onto the 5-mm mirror of a galvanometer (Y Galvo, Cambridge Technology, 6215H). Another pair of relay lenses ($f_1 = f_2 = 85$ mm) then image the SLM onto a second 5-mm galvo mirror (X Galvo, Cambridge Technology, 6215H). A final pair of relay lenses ($f_1 = 89$ mm and $f_2 = 350$ mm) creates a magnified image of the SLM at the rear pupil plane of the imaging objective (Nikon, CFI Apo LWD 25XW, 1.1 NA and 2 mm WD). Mutual conjugation of the SLM, both galvos and the objective rear pupil insures that the corrective phase pattern from the SLM is stationary at the objective rear pupil, even as the galvos scan the focused NIR light laterally across the specimen.

The visible excitation subsystem begins when four CW lasers ($\lambda = 440$ nm, 50 mW, CrystaLaser; $\lambda = 488$ nm, 200 mW, Coherent Sapphire 488 LP; $\lambda = 514$ nm, 300 mW, MPB Communications, model 2RU-VFL-P-300-514-R; and $\lambda = 561$ nm, 200 mW, Coherent Sapphire 561 LP) are expanded to a common a $1/e^2$ diameter of 2 mm and combined into a single colinear beam using dichroic beamsplitters (Semrock, LaserMUX family). An acousto-optic tunable filter (AOTF, AA Opto-Electronic, AOTFnc-400.650-TN) selects one or more wavelengths and controls the power of each. The linearly polarized output of the AOTF is expanded to a $1/e^2$ diameter of 10 mm, inserted into the microscope beam path using a dichroic beamsplitter (**Supplementary Fig. 1**, D2, Semrock Di01-R442/510 -25×36 or Di01-R488/561 -25×36) and reflected from a spatial light modulator responsive to visible light (SLM VIS, Boulder Nonlinear Systems, HSP256-0532). The SLM is used to apply the corrective pattern needed to retain both a diffraction-limited visible excitation focus in the specimen and a diffraction-limited focus of the fluorescence emission at a pinhole (50 μ m, Thorlabs, P50S) that provides filtering for the confocal imaging mode. This pinhole is manually removed when imaging in the two-photon mode. After passing through a polarizing beamsplitter (PBS, Thorlabs, PBS251), a pair of relay lenses ($f_1 = 150$ mm and $f_2 = 125$ mm) image SLM VIS onto Y Galvo. Thereafter, the path to the sample is shared with the NIR excitation. Consequently, SLM VIS, both galvos and the objective rear pupil are also mutually conjugate, and corrective phase pattern from SLM VIS is stationary at the objective rear pupil, even as the galvos scan the focused visible light laterally across the specimen.

In the fluorescence-detection subsystem, the focused fluorescence emission generated by either TPE or visible light is

collected by the objective and initially follows the reverse path of the NIR and visible excitation beams. After Y Galvo, however, another dichroic beamsplitter (D1, Semrock FF705-Di01 -25×36) diverts the emission through the relay lens pair that conjugates Y Galvo to SLM VIS. Half of this unpolarized light passes through PBS, reflects off SLM VIS and is focused by a lens of $f = 300$ mm before a photomultiplier tube (PMT, Hamamatsu, H7422-40 or R10467U-40). The signal from this detector forms the image in either the confocal or the TPE imaging mode, although the pinhole before the PMT is omitted in the latter. The other half of the fluorescence is reflected by PBS and is sent to the Shack-Hartmann (SH) wavefront sensor, positioned such that the lenslet array (10×10 lenses, 0.5-mm pitch, $f = 46.7$ mm, Edmund Optics, 64-483) is conjugate to the objective rear pupil and the two galvos. As a result, the detected light is descanned by the galvos, and a stationary wavefront is presented at the sensor, even as the focused excitation scans laterally across the specimen. Displacements of the foci on the SH camera (Andor iXon3 897 EMCCD) then solely represent the local wavefront gradients, as desired.

The choice of PBS to split the fluorescence signal equally between the SH sensor and the imaging PMT is an obvious one, given that SLM VIS requires linearly polarized light to modulate the phase properly. However, although this configuration is perhaps the simplest for an SLM-based system, the 50% signal loss at the PMT is a substantial price to pay. On the other hand, the question of the optimum split ratio is a complex one, as a number of factors influence how much signal the SH sensor requires to accurately measure the displacement of each lenslet-defined focal spot. Increasing the number of lenslets increases the complexity of the aberration that can be measured, but divides the SH signal among more elements. Decreasing the size of each AO corrective subvolume provides more local measurement of the aberration but decreases the total integrated signal collected for each such measurement. Finally, increased imaging depth generally leads to greater aberration and thus more dramatic improvement after AO correction, but it also results in more scattered background and less ballistic (focused) light at the SH sensor, requiring more signal to accurately measure the focal spot displacements. In short, the 50/50 ratio of the PBS configuration represents a simple compromise that works well for the specimens studied here, but other configurations, including a system with a variable split ratio, can be envisioned for other biological systems.

System calibration. Before measuring and correcting sample-induced aberrations, the microscope must be calibrated to compensate for its own aberrations. These arise from imperfect and/or misaligned optical components. We measure these system aberrations by the phase-retrieval method²¹, as it provides an independent means to determine the correction necessary to recover an ideal diffraction-limited focus for an ideal, nonaberrating point object.

To correct the aberrations in the visible light path, the pinhole near the PMT is removed, and a 3D image of an isolated, 200-nm diameter fluorescent bead on a glass slide is obtained by scanning the visible focus in a series of xy planes and stepping the sample in z to different planes with a piezoelectric flexure stage

(Physik Instrumente, P-622.2CD). The sampling interval must be smaller than the Nyquist limit

$$N_{x,y} = \lambda / (4NA),$$

$$N_z = \lambda / \left[2n(1 - \sqrt{1 - (NA/n)^2}) \right]$$

in each direction, and the field of view must be large enough that aberrated images of the bead (see below) are not cropped at the edges. The 3D image is then inspected, particularly for axial asymmetry indicative of spherical aberration, and the correction collar on the objective is adjusted. This process of 3D imaging and collar correction is repeated until the spherical aberration is minimized.

Next, the bead is moved to the *z* plane of best focus, and a series of seven 2D images are taken while applying seven different Zernike polynomial phase patterns²² of 2λ peak-to-peak amplitude on SLM VIS: flat phase, positive defocus, negative defocus, positive *x* astigmatism, negative *x* astigmatism, positive *y* astigmatism and negative *y* astigmatism. From these images, the wavefront correction for system aberration in the visible excitation path is retrieved using the Gerchberg-Saxton algorithm²¹. Thereafter, this pattern is applied to SLM VIS, and the wavefront correction for sample-induced aberrations is added to it to provide complete correction during normal operation.

To correct for aberrations in the NIR light path, a charge-coupled device (CCD) camera (AVT, Guppy F-146) is placed at the intermediate image plane located at the focus of the first relay lens after X Galvo. Seven 2D images of this focus are taken while applying the seven Zernike polynomial phase patterns listed above to SLM NIR, and the wavefront correction for system aberration in this portion of the NIR excitation path is retrieved using the Gerchberg-Saxton algorithm. Thereafter, this pattern is applied to SLM NIR, and the wavefront correction for sample-induced aberrations is added to it to provide complete correction during normal operation.

To calibrate the SH sensor, the visible and NIR wavefront corrections for system aberration are applied to SLM VIS and SLM NIR, respectively. A 2D image of a field of fluorescent beads is then taken in the two-photon imaging mode while integrating the signal at the SH camera. The resulting SH image consists of an array of foci, matching the elements of the lenslet array. The centroids of these foci are determined to subpixel precision and serve as the calibration reference. Thereafter, the displacements of these centroids from their reference positions indicate the local gradient of the sample-induced wavefront error, from which the wavefront itself can be calculated using a generalized matrix inversion method¹.

Note that all of the wavefronts presented in this work represent the corrections for sample-induced aberrations.

Image acquisition, wavefront sensing and adaptive optical correction. Because aberrations can vary rapidly as a function of position within biological samples, we image large volumes by dividing them into smaller subvolumes and determine an averaged AO correction unique to each subvolume. Stacked, closed-loop ultrasonic piezomotor stages (Physik Instrumente, M-663.465) are used initially for *xy* positioning of the sample to the focal point of the objective, as well as for lateral translation

between subvolumes. A closed-loop ball-screw-driven stage (Physik Instrumente, M-110.2DG) provides similar functions in *z*. Within each subvolume, X Galvo and Y Galvo scan the focus laterally, while a piezo flexure stage (Physik Instrumente, P-622.2CD) steps between scan planes to build a 3D image of the subvolume. At each voxel, the fluorescence photons reaching PMT generate current spikes that are first amplified (FEMTO Messtechnik GmbH, DLPCA-200) and then integrated over the pixel dwell time in a custom, fast-resetting analog integrator. The integrator output is digitized by an field-programmable gate array (FPGA)-based reconfigurable I/O board (National Instruments, PCIe-7852R) just before integrator reset from the same board at the end of the dwell period.

In the two-photon imaging mode, AO correction occurs simultaneously with image acquisition. The SH camera exposure time is chosen to be just long enough to yield an SNR sufficient to accurately measure the gradient of the wavefront. Calculation of the wavefront from this gradient occurs concurrently with the next SH exposure, and the resulting correction of sample-induced aberration is added immediately to the individual system corrections at SLM VIS and SLM NIR. Currently, the fastest closed-loop update time for new AO corrections is 14 ms, limited in bright samples by the readout speed of the electron-multiplying CCD (EM-CCD)-based SH camera. In the future, a scientific complementary metal-oxide-semiconductor (sCMOS) camera may permit faster correction.

In the confocal mode, AO correction occurs sequentially: in each corrective subvolume, the visible excitation is first blocked with the AOTF, the NIR light is passed by the Pockels cell and a fraction of the subvolume (often a single plane) is scanned by the TPE focus while the resulting descanned fluorescence is collected in a single exposure at the SH camera. After the wavefront correction is calculated and added to the system corrections at SLM VIS and SLM NIR, the NIR light is blocked and the visible light is passed in order to image the entire subvolume.

In either imaging mode, the aberration-corrected 3D point-spread function (PSF) of the microscope is first determined by imaging an isolated fluorescent bead (200-nm diameter) on a glass slide with system corrections applied to both SLMs. For regions of the sample where AO correction recovers near diffraction-limited resolution, these measured PSFs can be used to deconvolve the 3D imaging data using the Lucy-Richardson algorithm in Matlab. This provides a sharper 3D representation of the imaging volume that depicts the sample and the relative amplitudes of its spatial frequencies more accurately. Volume renderings of the data are created in Amira (FEI Visualization Sciences Group). For data sets with intensities covering a large dynamic range, a gamma function is often applied to visualize the dimmer features. (The imaging conditions and visualization parameters for all figures and videos are listed in **Supplementary Tables 1 and 2**).

Control electronics and timing. The EM-CCD camera that serves as the SH camera is set to internal triggering mode and serves as the master timing source—timing pulses from the fire out transistor-transistor logic (TTL) output of the EM-CCD are read by the FPGA card in a control computer (PC) to synchronize all operations (**Supplementary Figs. 8 and 9**). Analog outputs from the FPGA card provide user-defined waveforms that control X Galvo, Y Galvo and the Z sample piezo during imaging. These are conditioned by individual scaling amplifiers (SRS, SIM983, and

SIM900 mainframe) to match their 16-bit resolution to the control range of each device. Additional analog outputs to the Pockels cell and the AOTF control the intensity and blanking of the NIR and two selected wavelengths of visible light. A digital output synchronizes the integrator to the scanning, while an analog input digitizes the integrated signal at each voxel. All other hardware, including SLM NIR, SLM VIS, the coarse-ball-screw-driven *z* stage, the *x* and *y* ultrasonic piezo stages and a filter wheel are directly controlled by cards in the PC. The PC itself consists of a rack-mounted chassis with motherboard (Supermicro, SuperServer SYS-7046GT-TRF), dual microprocessors (Intel, Hexa-Core Xeon X5680 3.33 GHz 12 MB), 48 GB of RAM and a 1-TB hard drive running under 64-bit Windows 7 Pro. The entire microscope is controlled by custom 64-bit LabVIEW code (Coleman Technologies).

Zebrafish care and preparation. Wild-type and transgenic lines were maintained according to Institutional Animal Care and Use Committee of HHMI Janelia Farm. Zebrafish embryos were grown, staged and harvested as previously described^{23,24}. The following lines were used: roy^{a9}; gmc604Et; gmc930Tg, which expresses YFP in the membranes of a sparse set of neurons²⁵ (Fig. 1, Supplementary Fig. 7 and Supplementary Video 1); Tg(β -actin:mgfp), which expresses GFP in the membranes of all cells²⁶ (Fig. 2a and Supplementary Video 3); Tg(-4.9sox10:eGFP), which expresses eGFP cytosolically in a subset of oligodendrocytes in the brain^{27,28} (Fig. 2b–d, Supplementary Fig. 3 and Supplementary Video 2); Tg(-4.9sox10:eGFP) crossed with Tg(-8.4neurog1:nRFP), which expresses RFP in neuronal

nuclei²⁹ (Fig. 3 and Supplementary Video 4); s1101t-Gal4 (ref. 30) crossed with UAS-memCerulean, UAS-centrin2-YFP, which expresses YFP-tagged centrin2 in a broad subset of neurons, including in the retina (Supplementary Fig. 5a–e); and HuC-Gal4 crossed with UAS-mitoCFP/memYFP, which expresses CFP in the mitochondria and YFP in the plasma membrane of a broad subset of neurons³¹ (Supplementary Figs. 5f–h and 6 and Supplementary Videos 5 and 6).

Embryos were transferred at 12 h or 24 h after fertilization to E3 solution (5 mM NaCl, 0.17 mM KCl, 0.33 mM CaCl₂, 0.33 mM MgSO₄) containing N-phenylthiourea (Sigma) to inhibit pigmentation. For imaging, embryos were anesthetized using tricaine (Sigma) in E3 solution and mounted in 0.7% low-melting agarose (Sigma-Aldrich A4018) as described previously³².

21. Gerchberg, R.W. & Saxton, W.O. *Optik (Stuttg.)* **35**, 237–246 (1972).
22. Campbell, H.I., Zhang, S., Greenaway, A.H. & Restaino, S. *Opt. Lett.* **29**, 2707–2709 (2004).
23. Kimmel, C.B., Ballard, W.W., Kimmel, S.R., Ullmann, B. & Schilling, T.F. *Dev. Dyn.* **203**, 253–310 (1995).
24. Westerfield, M. *The Zebrafish Book: A Guide for the Laboratory Use of Zebrafish (Danio rerio)* 4th edn. (University of Oregon Press, 2000).
25. Xie, X. *et al. BMC Biol.* **10**, 93 (2012).
26. Cooper, M.S. *et al. Dev. Dyn.* **232**, 359–368 (2005).
27. Wada, N. *et al. Development* **132**, 3977–3988 (2005).
28. Carney, T.J. *et al. Development* **133**, 4619–4630 (2006).
29. Blader, P., Plessy, C. & Strahle, U. *Mech. Dev.* **120**, 211–218 (2003).
30. Szobota, S. *et al. Neuron* **54**, 535–545 (2007).
31. Plucińska, G. *et al. J. Neurosci.* **32**, 16203–16212 (2012).
32. Godinho, L. in *Imaging in Developmental Biology* (eds. Sharpe, J. & Wong, R.O.) Ch. 4, 49–69 (Cold Spring Harbor Laboratory Press, 2011).